Clinical Cancer Research

AACR

Discrete Molecular Classes of Ovarian Cancer Suggestive of Unique Mechanisms of Transformation and Metastases

Nilesh L. Gardi, Tejaswini U. Deshpande, Swapnil C. Kamble, et al.

Updated version	Access the most recent version of this article at: doi:10.1158/1078-0432.CCR-13-2063
Supplementary Material	Access the most recent supplemental material at: http://clincancerres.aacrjournals.org/content/suppl/2013/10/16/1078-0432.CCR-13-2063.DC1.html

Cited Articles	This article cites by 49 articles, 12 of which you can access for free at: http://clincancerres.aacrjournals.org/content/20/1/87.full.html#ref-list-1

E-mail alerts	Sign up to receive free email-alerts related to this article or journal.
Reprints and Subscriptions	To order reprints of this article or to subscribe to the journal, contact the AACR Publications Department at pubs@aacr.org.
Permissions	To request permission to re-use all or part of this article, contact the AACR Publications Department at permissions@aacr.org.

Human Cancer Biology

Discrete Molecular Classes of Ovarian Cancer Suggestive of Unique Mechanisms of Transformation and Metastases

Nilesh L. Gardi, Tejaswini U. Deshpande, Swapnil C. Kamble, Sagar R. Budhe, and Sharmila A. Bapat

Abstract

Purpose: Tumor heterogeneity and subsistence of high-grade serous ovarian adenocarcinoma (HGSC) classes can be speculated from clinical incidences suggesting passive tumor dissemination versus active invasion and metastases.

Experimental Design: We explored this theme toward tumor classification through two approaches of gene expression pattern clustering: (i) derivation of a core set of metastases-associated genes and (ii) resolution of independent weighted correlation networks. Further identification of appropriate cell and xenograft models was carried out for resolution of class-specific biologic functions.

Results: Both clustering approaches achieved resolution of three distinct tumor classes, two of which validated in other datasets. Networks of enriched gene modules defined biologic functions of quiescence, cell division-differentiation-lineage commitment, immune evasion, and cross-talk with niche factors. Although deviant from normal homeostatic mechanisms, these class-specific profiles are not totally random. Preliminary validation of these suggests that Class 1 tumors survive, metastasize in an epithelial–mesenchymal transition (EMT)-independent manner, and are associated with a p53 signature, aberrant differentiation, DNA damage, and genetic instability. These features supported by association of cell-specific markers, including PAX8, PEG3, and TCF21, led to the speculation of their origin being the fimbrial fallopian tube epithelium. On the other hand, Class 2 tumors activate extracellular matrix–EMT–driven invasion programs (Slug, SPARC, FN1, THBS2 expression), IFN signaling, and immune evasion, which are prospectively suggestive of ovarian surface epithelium associated wound healing mechanisms. Further validation of these etiologies could define a new therapeutic framework for disease management. *Clin Cancer Res; 20(1); 87–99. ©2013 AACR.*

Introduction

Rapid metastases and disease progression are a major cause of mortality in high-grade serous epithelial ovarian cancer (HGSC) and with which, a mechanistic association of epithelial to mesenchymal transition (EMT) is implied (1). The process of EMT involves cooperation of niche factors through autocrine–paracrine signaling with a transcriptional program driven by E12/47 (TCF3), TCF4, Twist, ZEB1, ZEB2, Snail (*SNAI1*), Slug (*SNAI2*), FOXC1, or FOXC2 (refs. 2, 3; collectively termed as EMT-TFs). Besides EMT, passive shedding, cooperative migration of multicellular aggregates from the surface of growing tumors, and peritoneal seeding (4), and associations of lysophosphatidic acid (LPA) and/or sphingosine 1-phosphate (S1P) signaling with HGSC metastases (5) are reported. The latter are increasingly being associated with cancer cell survival, tumor progression, angiogenesis, metastasis, and chemoresistance (6).

The ovarian surface epithelium (OSE), an innocuous, primitive mesothelium belies the fact that its transformation results in aggressive HGSC. Incessant ovulation and release of the ovum into the fallopian tubes leads to localized OSE injury and consequent healing through EMT and mesenchymal to epithelial transition (MET; 7, 8). Recently, involvement of FT distal fimbrial epithelial (FTE) transformation in HGSC was suggested based on similarities with Müllerian tract tumors (9, 10). Evidences and contradictions for both cells-of-origin exist; (i) a pathologic association of OSE-derived inclusion cysts and inflammation in association with cyclic ovulation-wound healing with HGSC is established (8, 11). However, higher level of differentiation in tumor epithelia than OSE contradicts the dogma of tumor-associated maturation arrest. (ii)

Authors' Affiliation: National Centre for Cell Science, NCCS Complex, Pune University Campus, Pune 411 007, Maharashtra, India

N.L. Gardi and T.U. Deshpande contributed equally to the *in silico* analyses.

S.C. Kamble and S.R. Budhe contributed equally to the wet lab experimentation.

Corresponding Author: Sharmila A. Bapat, National Centre for Cell Science, NCCS Complex, Pune 411007, India. Phone: +91-20-25708074; Fax: +91-20-25692259; E-mail: sabapat@nccs.res.in

American Association for Cancer Research **87**

Translational Relevance

Variations in gene expression patterns can be grouped to identify discrete molecular classes in cancer. Here, we identify and correlate high-grade serous ovarian adenocarcinoma (HGSC) tumor groups with distinct functional patterns that suggest differential mechanisms of transformation. We hope our findings will further lead to improved understanding and specific targeting of these tumors toward better disease management.

Oxidative stress, cell hyperactivation, and DNA damage in FTE lead to preneoplastic tubal intraepithelial lesions in p53/BRCA1/BRCA2 mutation harboring patients in whom prophylactic oophorectomy does not reduce risk of recurrence (12, 13); however, HGSC incidence in patients without these mutations remain unaccounted for. This conundrum suggests subsistence of at least 2 subtypes in HGSC that at present is diagnosed as a single disease based on clinical characteristics.

In the present study, we attempted tumor classification through two approaches; (i) supervised metastases-gene signature based clustering, and (ii) unsupervised, Weighted Gene Correlation Network Analysis (WGCNA) analyses. Both methods defined similar tumor groups in which molecular systems networks-based resolution of class-specific tumor-associated biologic functions revealed unexpected pathway associations. Class1 tumors survive, metastasize in an EMT-independent manner, and are associated with aberrant differentiation, genetic instability, and immune evasion. Their molecular profiles and cellular behavior suggest possible involvement of FTE and ovarian stroma. Class2 tumors express extracellular matrix (ECM)-EMT–driven invasive gene networks and IFN signaling that put forth a plausible cell-of-origin being the OSE. Preliminary validation of these suggestive etiologies was carried out in experimental models using distinctive markers purported to be associated with either the FTE (oxidative stress, DNA damage, genetic instability, and apoptosis) or OSE (EMT, ECM).

Materials and Methods

Derivation of the 39 metastases-associated gene signature

Level 3 high-grade ovarian serous cystadenocarcinoma gene expression data was extracted from TCGA (14; https://tcga-data.nci.nih.gov/tcga/tcgaHome2.jsp) from two platforms, *viz.* Affymetrix (512 tumor and 8 normal samples) and Agilent (359 tumor and 8 normal samples) as available on October 2010 (Supplementary Table S1). Data was Lowess normalized and log2 transformed. Further correlation analysis of EMT-TFs *SNAI1*, *SNAI2*, *TCF3*, *TCF4*, *TWIST1*, *ZEB*, and *ZEB2* with epithelial and mesenchymal markers involved applying Pearson correlation coefficient ($-0.5 < r < 0.5$; $P < 0.05$) followed hierarchical clustering of both datasets. ChIP-on-chip was carried out as described

earlier (15). Briefly, 10^8 cells (serous ovarian adenocarcinoma cell line - A4 established earlier in our lab; refs. 15, 16) were chemically crosslinked, harvested, lysed, sonicated to solubilize, and shear crosslinked DNA that was immunoprecipitated with Snail, Slug, or Twist antibodies, purified, labeled, and hybridized with Agilent human whole-genome promoter microarrays. Identification of global targets of Twist, Snail, and Slug was carried out using Agilent Genomic Workbench Lite version6.5.0.18; using a significance cutoff ($P < 0.05$). Expression levels of these genes were extracted from GSE18054 (gene expression profiles of A4 pretransformed and transformed cells). Genes with fold change (ratio of log intensity value between transformed and A4 pretransformed) expression value between 0 and 1 were considered low expressed and those with negative values were considered repressed. Furthermore, Pearson correlation coefficient ($-0.4 < r < 0.4$ with at least 2 gene partners; $P < 0.05$) was carried out in the A4 gene expression dataset. Finally, the 99 gene set that represented common targets of all three transcription factors were considered as EMT target genes. Using a similar approach, Pearson correlation analyses of known LPA and S1P associated receptors as well as components of LPA-S1P receptor-mediated signaling (identified from REACTOME, KEGG and Pathway Interaction Databases was carried out (http://www.reactome.org/ReactomeGWT/entrypoint.html, http://www.genome.jp/kegg/pathway.html, http://pid.nci.nih.gov/PID/index.shtml). The final list of metastases genes were subjected to median absolute deviation (MAD) analysis for highly differential genes [criterion ($-1 <$ fold change >1)] in at least 10% of samples) followed by Pearson correlation coefficient ($-0.4 < r > 0.4$ with at least 2 gene partners; $P < 0.05$) that identified 39 genes referred to as the 39 metastases-associated gene signature.

Classification of serous ovarian carcinoma samples based on core 39 metastases-related genes (M-classification)

We applied this 39 metastases-associated gene signature toward tumor classification using three methods, (i) Silhouette plots that identify silhouette-width–based clusters and associated outliers, (ii) Consensus average linkage clustering, and (iii) Hierarchical clustering. The 39 metastases-associated gene signature was applied for K-means classification of the cohort ($n = 359$) from $K = 2$ to $K = 6$ and silhouette plots were generated in which the Silhouette width (indicating clustering strength) is determined for each sample (17). Agglomerative average linkage hierarchical consensus clustering (R: ConsensusClusterPlus) was performed on positive silhouette width samples ($n = 329$) using a distance metric (1- Pearson correlation coefficient); the procedure was run over 1,000 iterations and a subsampling ratio of 0.8. Consensus clustering involves subsampling from a set of total tumor samples through calculation of pairwise consensus values based on the probability that two samples occupy the same cluster out of the number of times they occurred in the same subsample (18). A consensus matrix was the summarized form of all

pairwise consensus values that then cluster over number of iterations. Unsupervised Principle Component Analyses (PCA) was carried out for class resolution, whereas Between Group Analyses (BGA) was performed to identify class-specific gene–sample association. Common tumor samples from the two methods were further subjected to hierarchical clustering.

Weighted gene co-expression network analysis (WGCNA) and module identification (W-classification)

For details, see Supplementary Data S1 and Refs. 19, 20.

Validation of molecular classes, modules, and genes in additional Ovarian Cancer datasets

For details, see Supplementary Data S2.

Identification of class-defining features using Gene Set Enrichment Analysis

Gene set enrichment analysis (GSEA; ref. 21) was performed to identify enriched gene sets at $P < 0.1$ and $q < 0.25$. Class comparison networks were visualized using Enrichment map in Cytoscape_v2.8.2. Application of GSEA identified some biologic processes and signaling pathways ($P < 0.05$; FDR < 0.25).

Cell culture, RT-PCR, *in vitro* Scratch assay, and three-dimensional cultures

Cells were cultured as per the American Type Culture Collection guidelines. Reverse transcriptase-PCR (RT-PCR) for highly co-relating genes of the top 25 list of each module was done as described earlier (1) using GAPDH as an internal control. Fold change > 1.0 was considered significant. Relative gene expression was plotted as a heatmap using MeV. Scratch assay was carried out as described (1); in brief, cells were grown till confluency and a wound was inflicted with a pipette tip. Subsequently two washes with 1XPBS were given to remove floating cells and media with additives was added. Additives to basal medium include FBS (5%), EGF (10 ng/mL), TGF-β (10 ng/mL), S1P (5 μmol/L), LPA (5 μmol/L), FBS (5%) + LPA (5 μmol/L). Images captured on Olympus IX71 microscope and analysed by TScratch Software (22). Significance of relative wound area covered for respective time points was determined by one way ANOVA using Bonferroni test. For three-dimensional growth analyses, cells were cultured in suspension (in ultra low adherent dishes for suspended culture in medium devoid of serum) or in Matrigel (23); clumps of 4 to 10 cells were obtained by dislodging cells through scraping and gentle pipetting. Cell clumps were observed under microscope for size and cell number counted. Larger clumps were fragmented by pipetting. At day 4 and 9, spheroids were fixed and immunofluorescence stained. Images were captured, using CellD image capture software.

Cell-specific markers, immunofluorescence, and immunohistochemistry

Cell line models were immunostained for cell-specific expression markers MET (TCF21), EMT (Slug), ovarian stroma (PEG3) and secretory FTE (PAX8). Immunofluorescence staining and imaging was carried out as described earlier (15). In brief, cells grown on coverslips were fixed, blocked with 5% bovine serum albumin (BSA), and incubated with primary antibody for 1 hour. After two washes, cells were probed with labeled secondary antibody. Animal experimentation was done in accordance with the rules and regulations of the National Centre for Cell Science (NCCS) Institutional Animal Ethics Committee (IAEC). Xenografts were raised as described earlier (15). In brief, 2.5×10^6 cells were injected in nonobese diabetic/severe combined immunodeficient mice subcutaneously in the thigh. Animals were maintained under pathogen-free conditions and tumor growth assessed every 2 days until the tumor diameter was approximately 1 cm, whereupon animals were sacrificed to harvest tumors.

Expression of TCF21, Slug, PEG3, PAX8, and ECM molecules THBS2, SPARC, FN1 was assessed in three xenograft models per cell line. In brief, sections were deparafinized, hydrated, then blocked with 5% BSA and incubated with primary antibody overnight. Next day, sections were incubated with secondary antibody, HRP-conjugate (Invitrogen), and color developed by DAB (Pierce). After counterstaining with hematoxylin (Sigma), sections were dehydrated, paraffinized, and mounted. Dilutions of primary and secondary antibodies used were as recommended.

Genomic instability, oxidative stress, and mutational study

Genomic instability was assessed by Immunofluorescence staining of (α-tubulin, H2AX pericentrin, Hoechst) in cell lines and xenograft models. Ten to 15 nuclei from 10 fields were randomly chosen and scanned for identifying different types of mitotic and cell division abnormalities and determining percent frequency of each aberration. Profiling of cellular Glutathione [GSH; determined by flow cytometry of monochlorobimane (Invitrogen) stained cells], H2AX, and Annexin V-FITC was carried as described earlier (24). In brief, 10^6 cells were incubated with 25 μmol/L monochlorobimane for 30 minutes at 37°C, washed twice with $1\times$ PBS, and intensities acquired using Amcyan filter on Canto II flow cytometer (BD). Since GSH acts as a primary antioxidant, its intracellular levels are often assayed as a measure of reactive species of oxygen (ROS) and nitrogen (RNS) in cells that lead to oxidative stress. Thus, we assayed GSH levels through competitive binding of Mono-ChloroBimane (mBCl) to glutathione-S-transferase (GST) that is involved in the oxidation of GSH by ROS and RNS. Lower levels of mBCl-GST indicate more ROS (as seen in OVCAR3 than in A4 cells), which in turn can induce DNA damage and increased H2AX foci formation. Profiling for DNA damage and apoptosis achieved through profiling H2AX and Annexin V-FITC as described. In brief, cells were fixed with 4% paraformaldehyde, permeabilized using 2% Triton X, blocked with 10% goat serum for 20 minutes, incubated with primary antibody for 30

minutes and secondary antibody for 20 minutes. H2AX was added to a final concentration of 1 µg per 1 million cells. A minimum of 10,000 cells were analyzed for each dataset and fluorescence intensities were measured on a logarithmic scale of fluorescence of four decades of log. Data were collected, stored, and analyzed with the FAC-Station software (BD Biosciences). BRCA1 and BRCA2 specific oligos were designed for amplification of genomic DNA; amplification products were processed for Sanger sequencing as described earlier (25). Primer sequences are available on request.

Results

Resolution of discrete molecular classes in serous ovarian adenocarcinoma

Tumor stratification was achieved using two approaches for gene expression pattern clustering, derivation of a core set of metastases-associated genes, and resolution of independent weighted correlation networks.

Derivation of a 39 metastases-associated gene signature, stratification, and identification of core tumor samples in each class (M-classification). Expression of five EMT-TFs *TCF4*,

TWIST1, *SNAI2*, *ZEB1*, and *ZEB2* correlated positively with *Vimentin* (mesenchymal marker) and each other; and negatively with *CDH1*, *KRT8*, *KRT18* (epithelial markers) in the serous ovarian adenocarcinoma data across two platforms (Affymetrix and Agilent) in The Cancer Genome Atlas Research Network (TCGA; Supplementary Table S1; Fig. 1A and Supplementary Fig. S1A; ref. 24). Twist, Snail, and Slug global targets were identified through genome-wide ChIP-on-chip. Significant enriched target probes and genes ($P < 0.05$) were identified for each transcription factor and correlated with their expression levels (extracted from GSE18054, the A4 gene expression dataset generated and deposited by us with GEO; refs. 26, 27) to identify repressed genes (strong targets) and genes with low level expression (that may possibly result from a dose dependent regulation and hence are considered as weak targets). Thus, 58 repressed and 135 low expressed Slug target genes; 91 repressed and 206 low expressed Snail target genes; and 107 repressed and 200 low expressed Twist target genes were identified (Supplementary Fig. S1D). Of these, only 33 repressed genes and 66 low expressed genes harbored an E-box (CANNTG, the consensus sequence recognized by the
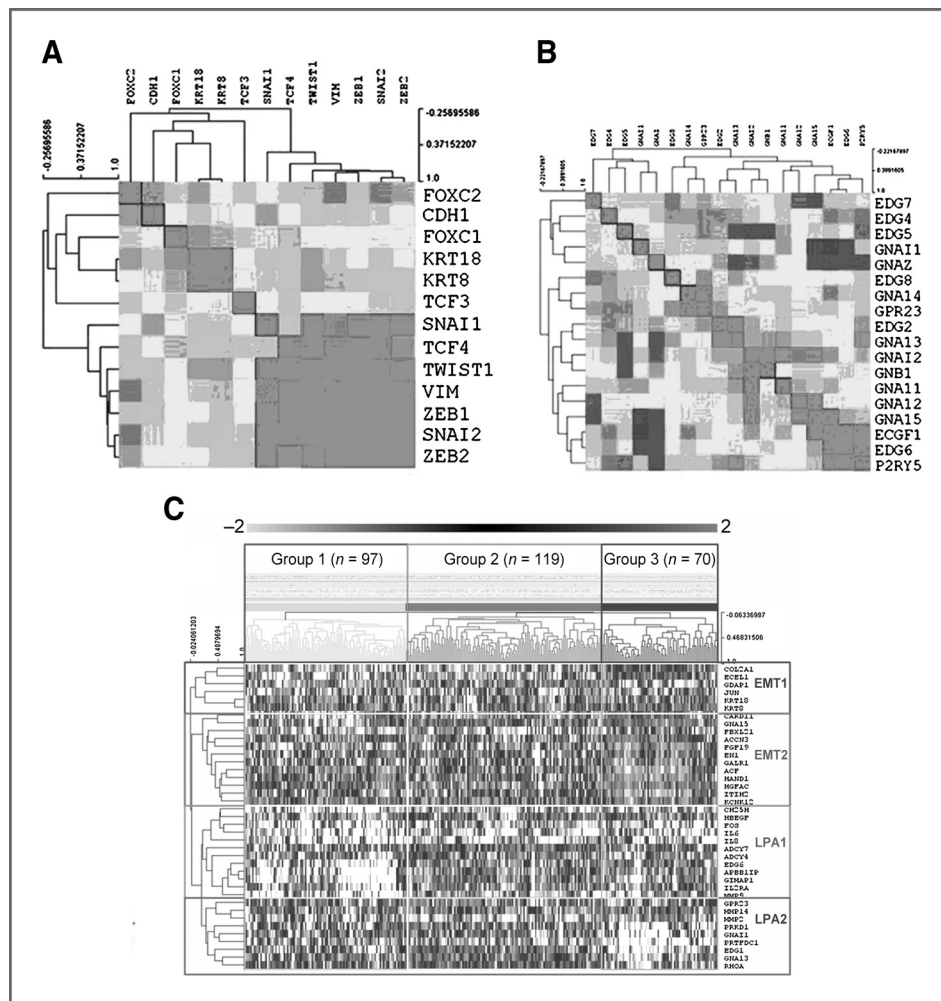
Figure 1. Derivation of the 39 metastases-associated gene signature (A and B) Pearson correlation (*r*) maps of EMT related transcription factors using Agilent data (A; $-0.5 < r < 0.5$; $P < 0.05$). B, LPA-S1P mediated signaling associated genes; C, between group analysis (BGA) depicting 39 gene expression profiles in 3 clusters; D, heatmap of 39 metastases-associated gene signatures between Class 1, Class 2, and Class 3 samples.
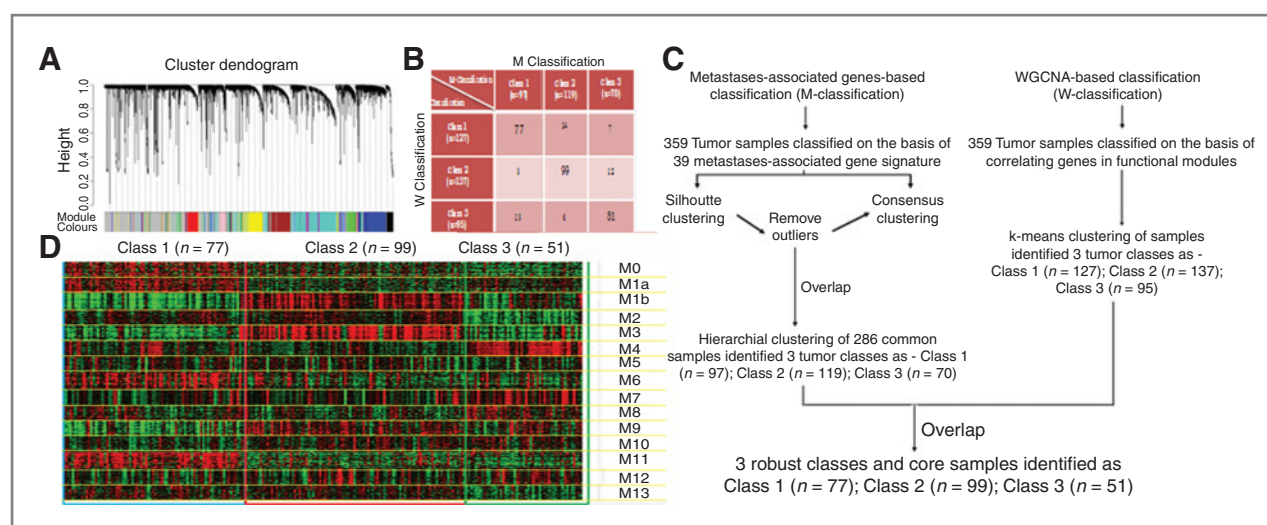
EMT-TFs), either within the probe or 500 bp up- and downstream of the probe. These 99 common target genes constitute the consolidated EMT targets in this study (Supplementary Table S2). Toward exploring the effects of LPA-S1P receptor–mediated signaling, an initial listing of the components was derived by manual literature annotation and from the REACTOME, KEGG, and Pathway Interaction Databases (http://www.reactome.org/ReactomeGWT/entrypoint.html, http://www.genome.jp/kegg/pathway.html, http://pid.nci.nih.gov/PID/index.shtml). This was followed by Pearson correlation analysis ($0.4 < r > -0.4$) across TCGA Affymetrix and Agilent platform generated data, to establish their relevance to serous ovarian adenocarcinoma. Thereby, 61 LPA-S1P associated and strong correlating genes were revealed (Fig. 1B and Supplementary Fig. S1B; Supplementary Table S2). Further hierarchial clustering, median absolute deviation (MAD) analyses and Pearson correlation between these 160 (99 EMT + 61 LPA-S1P) genes led to the derivation of a core set of 39 EMT-LPA-S1P signaling genes (Table 1; Supplementary Fig. S3).

Clustering identified class-specific gene-sample association and assigned a projection to each sample within individual classes (detailed in Supplementary Fig. S2). Class comparison between the silhouette- and consensus-based clustering suggested a high degree of overlap (Supplementary Fig. S1C) and further reaffirmed in hierarchical clustering. Unsupervised principle component snalyses and between group analyses lent support through similar class resolution and class-specific gene–sample associations (Fig. 1C and Supplementary Fig. S1C). The class-specific distribution of 286 samples classified was - Class1 (97), Class2 (119), Class3 (70; Fig. 1D).

Weighted gene co-expression network analysis and module identification (W-classification). Concurrently, we evaluated a metastases-independent classification scheme using Weighted Gene Correlation Network Analysis (WGCNA) that determines Pearson correlation coefficients across all possible pairs of genes by generating an adjacency matrix and organizing expression intensities to identify unique functional modules of highly correlating genes (28). Applying such a matrix at power 6 (weighted correlation =

Table 1. Derivation of 39 metastases-associated gene set through statistical analysis of EMT target genes identified through ChIP-chip and LPA-S1P signaling components

		85 Genes				39 Genes	
		JUN	EGFR	IL6		JUN	GNA15
		ACCN3	EN1	IL8		ACCN3	GNAI1
		ACF	F10	ITIH2		ACF	GPR23
		ADCY2	FAM19A4	KCNK12		ADCY4	HAND1
		ADCY3	FBXL21	KCNK17		ADCY7	HBEGF
		ADCY4	FGF19	KLHL1		APBB1IP	HGFAC
		ADCY7	FLT3	KRT18		CARD11	IL2RA
		ADCY8	FOS	KRT8		CH25H	IL6
		ADRA2B	GAB1	MMP14		COL2A1	IL8
		ALDH3A1	GALR1	MMP2			
99 EMT	APBB1IP	GDAP1	MMP9		ECEL1	ITIH2
targets + 61	Median Absolute	ASCL2	GIMAP1	MYH11	Pearson Correlation	EDG1	KCNK12
LPA – S1P	Deviation	BCL2L14	GLULD1	NOL4	coefficient	EDG6	KRT18
receptor events	———→	BHMT	GNA13	NPPC	———→	EN1	KRT8
(See Methods	Criteria	CACNA2D1	GNA14	NXPH2	$0.4 < r > -0.4$	FBXL21	MMP14
for details)	($-1 <$ fold				with at least 2	FGF19	MMP2
	change >1)	CARD11	GNA15	PAEP	gene partners	FOS	MMP9
	In at least 10%	CDH1		PIK3R1		GALR1	PRKD1
	of samples	CH25H	GNAI1	PRDM14		GDAP1	PRTFDC1
		CHST9	GNAZ	PRKCD		GIMAP1	RHOA
		COL2A1	GNMT	PRKD1		GNA13	
		CRTAC1	GPR23	PRTFDC1			
		CTNND2	HAND1	RET			
		CYB5R2	HBEGF	RHOA			
		DGKI	HES5	SLC1A2			
		ECEL1	HGFAC	SLC9A3R2			
		EDG1	HOXA4	ST6GALNAC5			
		EDG2	IL17B	TIAM1			
		EDG6	IL2RA	TMEM16A			
		EDG7					

Figure 2. A, Gene dendrogram obtained by average linkage hierarchical clustering; the color row underneath the dendrogram shows the module assignment determined by the Dynamic Tree Cut. Each module is defined as cluster of positively correlated genes fall into single branch of dendrogram and assigned a distinct color; gray lines represent unclassified genes listed as Module "0" (Supplementary Data S1, Supplementary Table S1); B, core tumor samples identified using overlap of two classification schemes *viz*. M-classification and W-classification ($P < 2.2 \times 10^{-16}$, Fisher exact test); C, flowchart summarizing metastasis classification and WGCNA classification approaches; D, heatmap of core tumor samples and Top 50 genes from each WGCNA module. Red and green colors correspond to upregulated and downregulated genes, respectively.

correlation[6]) to a core list of 6,840 significant genes generated 13 exclusive *Blockwise Modules* on the dendrogram using Dynamic Tree Cut algorithm (Fig. 2A). The detailed WGCNA methodology is provided as Supplementary Data S1; modules and genes listed in Supplementary Table S4; M0 represents genes unassigned to any module. Each module comprised of genes with high inter-connectedness and an expression pattern distinct from other module genes as revealed in the Topological Overlap Matrix plot (Supplementary Data S1 and Supplementary Fig. S1A).

K-means clustering in conjunction with Top 25 highest correlating genes from all modules led to the resolution of 3 tumor classes (Class1-127, Class2-137, Class3-95; Supplementary Data S1 and Supplementary Fig. S1B). A striking feature that was observed related to the similar distribution of specific tumor samples in the metastases- and WGCNA-based classifiers (Fig. 2B). This encouraged us to extract the core samples through an overlap of two approaches (Class1-77; Class2-99; Class3-51; Supplementary Data S1 And Supplementary Fig. S2) that were considered in the further analyses. A flow-chart of the derivation of these three classes and enriched samples is summarized in Fig. 2C.

Identification of class-specific module expression and validation in other datasets

Further derivation of a comparative median expression profile graph and heatmap of the common samples resolved class-specific functional module associations. Thus, enrichment of modules M1a, M6, M11 in Class1, that of M1b, M3, M9 in Class2, and M2, M4 in Class3 respectively was identified (Supplementary Data S2 and Supplementary Fig. S2; Fig. 2D). On profiling the distribution of 39 metastases-associated genes across the module

genes, it was seen that LPA-S1P genes were represented in M1b and M3 (Class2), whereas EMT-TF targets were represented in M4 (Class3; Supplementary Data S1 and Supplementary Table S2). Toward further independent evaluation of the predicted class-module associations across platforms and data in different submissions, we assessed the same in 7 other publicly available datasets (Supplementary Data S2). Briefly, the Top 50 genes from enriched modules were used for clustering and class identification; these classes and module associations were further statistically affirmed through rigorous Module Preservation Analysis.

Class1 and Class2 module associations validated well and network based preservation statistics (*Z* summary and medianRank) of these across all datasets indicated a strong preservation of modules M1a, M1b, M3, M6, M9, M11. However, an inconsistent correlation of M2, M4 genes with Class3 tumors and poor module preservation statistics in the validation datasets led us to discontinue Class3 from further analyses. We also affirmed the gene exclusivity within enriched modules in Class1 and Class2 tumors through profiling of their interactor networks in ARACNe (29). Within a tumor class, each module displayed strongly coregulated nodes and their hubs of influence besides exhibiting intermodular connectivity through a few hub components (Fig. 3A and B), that could possibly identify cross-talk and regulatory features.

Enriched modules assign distinct biological functionalities to two tumor classes

We further speculated the anticorrelative expression patterns of modules M1a-M6-M11 (Class1) and M1b-M3-M9 (Class2) tumors (Fig. 3C) to possibly instruct class-defining features. An initial exploration using GSEA (21) indeed
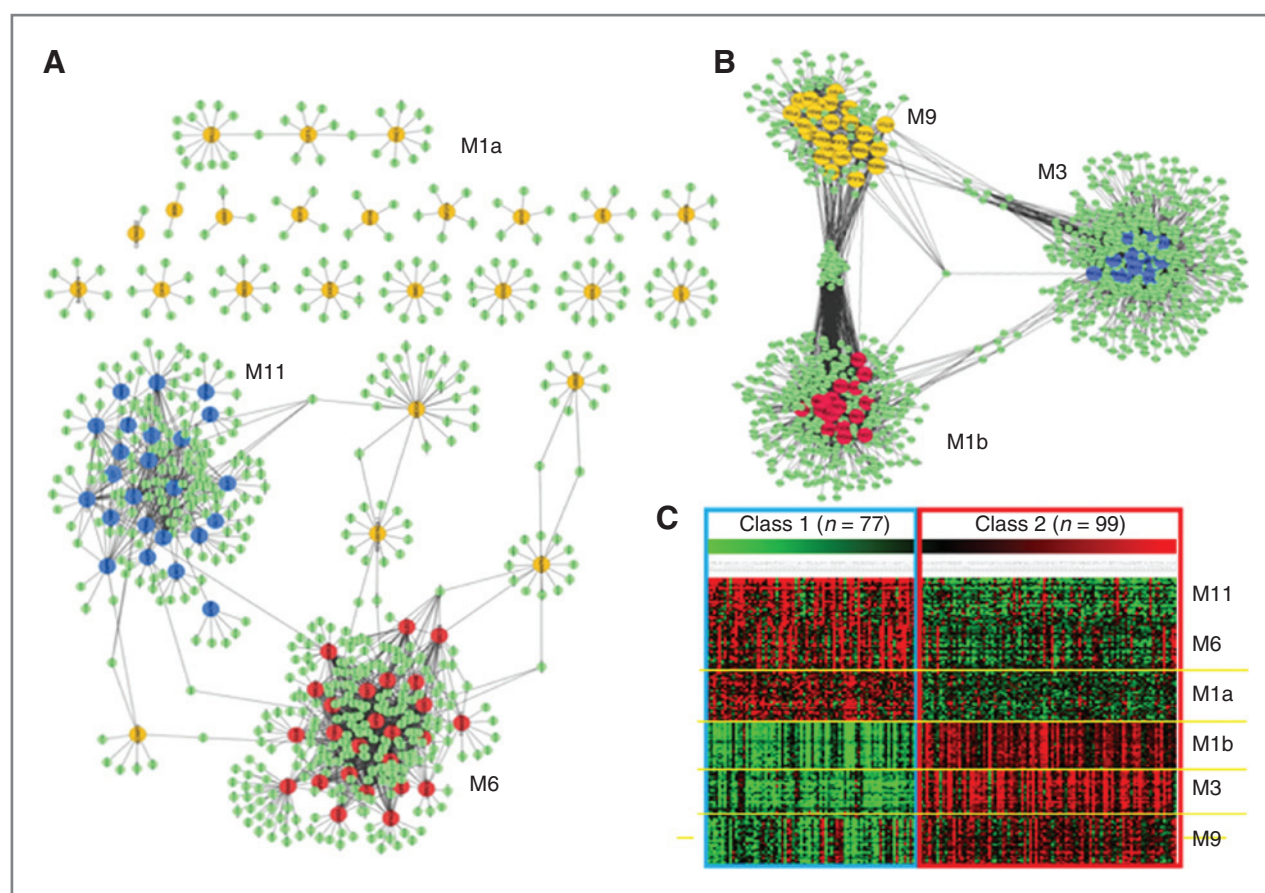
Figure 3. ARACNe-based predicted of interactive networks of enriched module genes (interactions with each other and with predicted targets). A, Class1 M1a genes (yellow circles), M6 genes (red circles), M11 genes (blue circles), predicted targets (green circles). B, Class2 M1b genes (red circles), M3 genes (blue circles), M9 genes (Yellow circles), predicted targets (green circles). C, representative heatmap of expression intensity of enriched module genes in the two tumor classes.

revealed class-specific biologic functions that unfortunately were not too comprehensive (Supplementary Data S3). We thus resorted to detailed literature-based functional annotation of Top 50 genes in enriched modules to identify functional class associations (Supplementary Table S5).

In Class1 tumors, M1a genes are involved in altered chromatin remodeling; Wnt and HH signaling; metastases; regulation of quiescence, cell-cycle and differentiation; cell lineage commitment toward adipogenesis, chondrogenesis, myogenesis, neurogenesis, and spermatogenesis. M6 genes represent 3 functional categories, (i) Cancer Germline/Testes Antigens (*CGA/CTA*), whose association with meiosis and unexpected expression in tumors suggests abnormal chromosome segregation (aneuploidy), (ii) Cilia and Dynein related genes essential for ciliary architecture and mitotic spindle stability, (iii) Tumor suppressor genes. M11 genes are associated with integral ovarian functions, including steroid hormone biosynthesis, metabolism, stem cells, and epithelial differentiation.

Within Class2 modules, M1b genes define either hematopoietic cell surface molecules linked to inflammation, innate/adaptive immune mechanisms, or escape of tumor

cells from immunosurveillance. M3 genes include extracellular matrix (ECM), EMT-associated, and dedifferentiation signature components known to be associated with TGF-β, PDGFRB, and Wnt signaling. Some M9 genes are components of the immunoproteasome and HLA Class I/Class II molecules involved in antigen processing and presentation while others define interferon networks (either being regulated by interferons or trigger their production) to mediate diverse biologic effects, including apoptosis, endothelial progenitor regulation, early immune stress response, post-translational modifications (ubiquitination, DNA damage-dependent PAR), immune tolerance, and survival.

The above networks thus impart unique identities to the tumor groups in support of their being defined as molecular classes. Further validation of predicted biologic functions necessitates development of appropriate experimental models *vis-à-vis* class-specific cell lines that could serve to be convenient validation tools. On generating gene expression data-based silhouette plots of eight human serous ovarian adenocarcinoma cell lines (Supplementary Table S6) along with the TCGA tumors, it was observed that OAW42, OVCAR3, HEY, OV90, 2008 patterns clustered
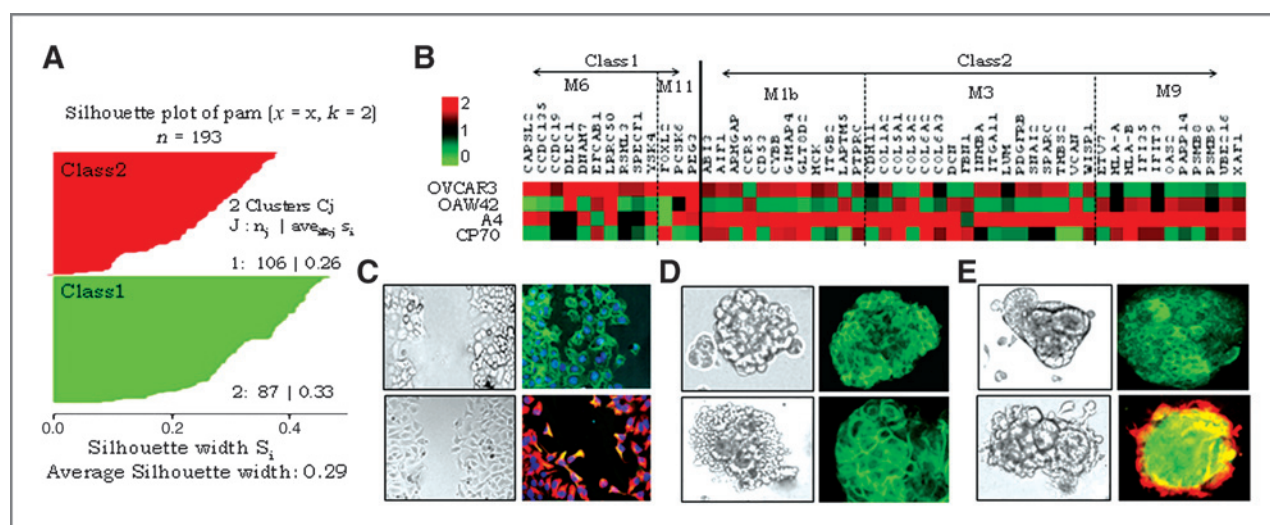
Figure 4. Identification of experimental models for validation of class-specific features. A, silhouette plot of Class1 ($n = 87$) and Class2 ($n = 106$) samples with serous ovarian carcinoma cell lines using top 50 module genes at $k = 2$ k-means clustering; B, heatmap showing expression values (RT-PCR) of module gene for the 4 cell lines normalised with GAPDH; C, representative phase contrast (left) and immunofluorescence (right) images of Scratch assay - OVCAR3 and A4 at 144 and 24 hours post-wounding, respectively; D, (i) 4-day-old, 3-dimensional suspension cultures of OVCAR3 and A4; phase contrast (left) and immunofluorescence (right); (ii) 9 day-old three-dimensional cultures of OVCAR3 and A4 in Matrigel. For C and D, top, OVCAR3 (Class1), bottom, A4 (Class2), Immunostaining performed using E-cadherin (Alexa488-green), Vimentin (Cy3-red) antibodies, Nuclei stained with Hoechst.

with Class1 while those of A4, CP70, SKOV3 clustered with Class2 tumors, albeit SKOV3 being represented as an outlier (Fig. 4A). The availability and an earlier familiarity of handling OAW42, OVCAR3 (Class1) and A4, CP70 (Class2) cells in our lab led to their selection in validation. The predicted expression patterns concurred fairly within the 4 cell lines tested (Fig. 4B).

ECM–EMT cross-talk and invasion is a Class2 specific characteristic

Module M3 (enriched in Class2) functions suggest niche-epithelial interactions that link an altered microenvironment milieu with transcriptional regulation in tumor cells primarily mediated by the EMT-TF Slug. This presents a major differential modality of metastases between the two tumor classes, that was confirmed through the following assays:

(i). *In vitro* scratch assays—OVCAR3 and OAW42 (Class1) and A4 and CP70 (Class2) cells demonstrated differential invasive behavior *vis-à-vis* time required for wound healing, growth characteristics at the migratory edge, and growth factor influences. Both Class1 cells required around 120 to 144 hours in the absence of media supplements to heal at least 80% of the wound; A4 and CP70 cells were more efficient and achieved complete wound healing within 48 and 96 hours, respectively under similar conditions (Supplementary Figs. S4 and S5). The response of Class1 cells was enhanced by FBS + LPA, whereas that of Class2 cells was maximally triggered by EGF, TGF-β, FBS+LPA (alone or in combination). An important qualitative difference between the two classes was that

wound healing in Class1 cells was effected exclusively through rapid cell proliferation that achieved extension of the scratch edge into the wound without dissolution of cell junctions; whereas A4 and CP70 cells at the scratch edge undergo EMT, actively migrate into and proliferate to swiftly fill up the wound. In support of these observations, lack of vimentin and strong expression of E-cadherin was seen in OVCAR3 cells, whereas strong vimentin with lowered E-cadherin expression was observed in A4 cells (Fig. 4C).

(ii). Evaluating influence of ECM components on tumor behavior in non-adherent cell systems - Monitoring the growth of representative cells in suspension culture (no ECM), or ECM-enriched Matrigel-based sandwich cultures revealed novel effects of niche-tumor cell cross-talk. Single, suspended Class1 cells in either culture system failed to divide and underwent apoptosis within 10 to 12 days. However, when seeded as groups of 4 to 10 cells with intact cell junctions, they proliferate to generate compact, organized noninvasive spheroids in both systems, in which, a continual expression of E-cadherin but not vimentin is associated with these spheroids (Fig. 4D). In direct contrast, single Class2 cells survive, proliferate in both culture systems, and generate invasive mesenchymal cells as well as multicellular spheroids. The former settle/invade and form colonies at the bottom of the culture dish (Supplementary Fig. S6). Suspended Class2 spheroids in liquid culture are compactly organized, express E-cadherin but not vimentin—representative of MET (30). Spheroids in Matrigel range from small-compact, irregular-stellate, or large-organized shape and have invasive, vimentin-

expressing cells at their borders (Fig. 4D, ii). All effects were more pronounced in A4 cells. The differential behavior between the two classes lend strong support to the purported correlation of Class1 being EMT-deficient and Class2 being EMT-enabled.

Class1 cells are associated with a higher frequency of genetic instability

We proceeded to probe the differential effects of M1a genes (chromatin remodeling, cell cycle) and M6 genes (Cancer Testes Antigens, dyneins, tumor suppressors) that are preferentially enriched in Class1 over Class2, on altered cell cycle/division. This was carried out in OVCAR3 (Class1) and A4 (Class2) cells that were preferred due to a shorter latency periods of tumor generation in mouse models over OAW42 and CP70 xenografts. Immunofluorescence staining (α-tubulin, pericentrin, Hoechst) revealed more frequent anomalies of chromosomal and nuclear material rearrangements, including aberrant metaphase chromosome alignments, multipolarity, lagging anaphases, ring-shaped chromosomes, micronuclei, and multinucleation following cytokinesis defects in OVCAR3 than A4 cells in culture and in tumors (Fig. 5A, i and ii). While a higher frequency of metaphases in OVCAR3 tumors suggest them
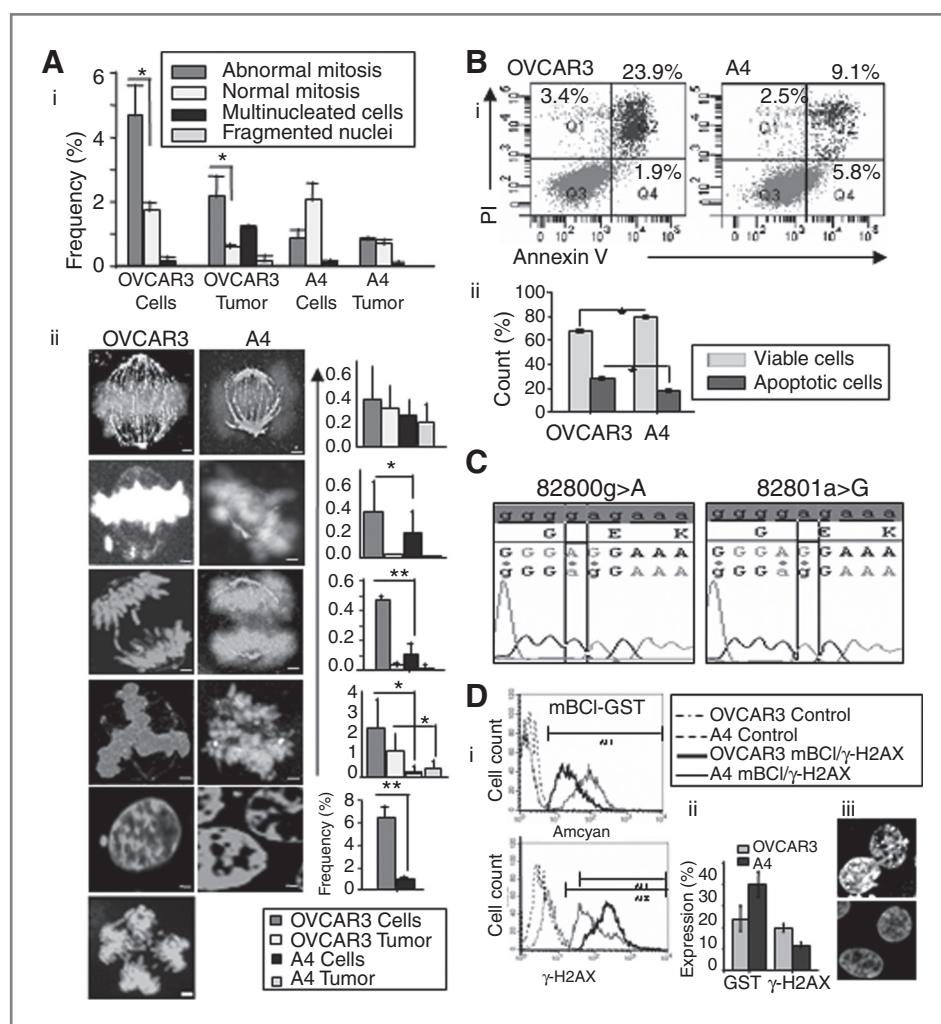
Figure 5. Profiling of experimental models for Class1-specific features (A) Genetic instability - the Y-axis in graphs represents the percent frequency of nuclear events (i) frequency of normal and abnormal mitosis, multinucleation and nuclear fragmentation in Class1 (OVCAR3) and Class2 (A4) models (cultured cells and xenograft tumors); (ii) representative images of various mitotic events (left; scale bar 5 μm), including (from top to bottom rows) normal metaphases, misaligned metaphase chromosomes, anaphase bridges, multi-polar spindles, micronuclei, cytokinesis abnormalities; cells stained with α-tubulin (green), pericentrin (red), and Hoechst (blue); bar graphs on right of each row represent percent frequency of same. Cytokinesis defects were rare events seen only in OVCAR3 cells; frequency not determined. B, representative dot plots (i) and graphs (ii) of flow cytometry–based quantification of Annexin V-FITC staining in OVCAR3 and A4 xenograft tumors indicating frequency of apoptosis (*$P < 0.05$). C, electropherograms depicting nucleotide changes in *BRCA2* at 82800g>A and 82801a>G that lead to an amino acid change E3256R in OVCAR3 cells. Reference nucleotide and amino acid sequences are indicated at the top. D, ROS generation and γ-H2AX in OVCAR3 and A4 cells (i) flow cytometry based quantification of cellular glutathione (GSH) expressed as change in monochlorobimane–glutathione-*S*-transferase (mBCl-GST) complex (top) and γ-H2AX (bottom), lower mBCl-GST levels indicate higher ROS; (ii) graphical representation of the same ($n = 3$); (iii) representative γ-H2AX expression (Red-Cy3) in OVCAR3 (left) and A4 (right) nuclei.

to be proliferative, increased nuclear fragmentation and apoptosis leads to delayed tumor latency and growth in these tumors over Class2 xenografts [Fig. 5A (i) and B]. Together, the data suggest more frequent cell-cycle defects and genetic instability in Class1 tumors.

Class-specific features suggest a discrete cell-of-origin to the two tumor classes

A p53 signature, BRCA1/BRCA2 mutations, oxidative stress–driven DNA damage, genetic instability, and cell hyperactivation define the recently identified etiology of preneoplastic fallopian tube intraepithelial lesions leading to HGSC (6, 7) that challenged the existing dogma of the OSE being its cell-of-origin. Considering this conundrum in view of the differential biologic behavior of the two tumor classes, we speculated the etiology of Class1 and Class2 tumors to be the FTE and OSE respectively, and delved deeper into class-specific features in searching for proof-of-concept support as follows:

(i) p53-signature—Mutated p53 is widely associated with HGSC (24); OVCAR3 established from a sporadic case of HGSC has been earlier associated with a loss-of-function p53 mutation (31), whereas A4 harbors wild-type p53 (26). Accumulation of nuclear p53 is also evident in these tumors along with DNA damage (γ-H2AX) and a high proliferative index (Ki-67; Fig. 6A)

(ii) BRCA1-BRCA2 mutational status—Novel point mutations in BRCA2 leading to nucleotide alterations 82800g>A and 82801a>G in exon 27

were identified in OVCAR3 cells that effect the non-synonymous amino acid change E3256R (Fig. 5C). This site lies in the RAD51 binding domain of the protein, which is critical for its functionality in DNA repair (32).

(iii) Oxidative stress-DNA damage—We probed this purported etiologic linkage in both cell systems by profiling their intrinsic ROS and γ-H2AX expression (early DNA double-stranded break, DSB marker). Since glutathione (GSH) acts as a primary antioxidant, its intracellular levels are often assayed as a measure of ROS and RNS in cells that lead to oxidative stress. Thus, we assayed GSH levels through competitive binding of Mono-ChloroBimane (mBCl) to glutathione-S-transferase (GST) that is involved in the oxidation of GSH by ROS and RNS. Lower levels of mBCl-GST indicate more ROS (as seen in OVCAR3 than in A4 cells), that in turn can induce DNA damage and increased H2AX foci formation. As seen from the assays, both effects *viz.* higher ROS levels (lower levels of GSH) and DNA damage (γH2AX foci formation) were more pronounced in OVCAR3 than A4 cells (Fig. 5D, i–iii). Complementation of DSB with the earlier observed cell cycle and division defects also were more frequently observed in OVCAR3 than A4 cells, and suggest an intrinsic DSB propensity possibly triggered through an upstream release of ROS that together with the p53 and BRCA2 mutations ultimately culminates in genetic instability in these cells.
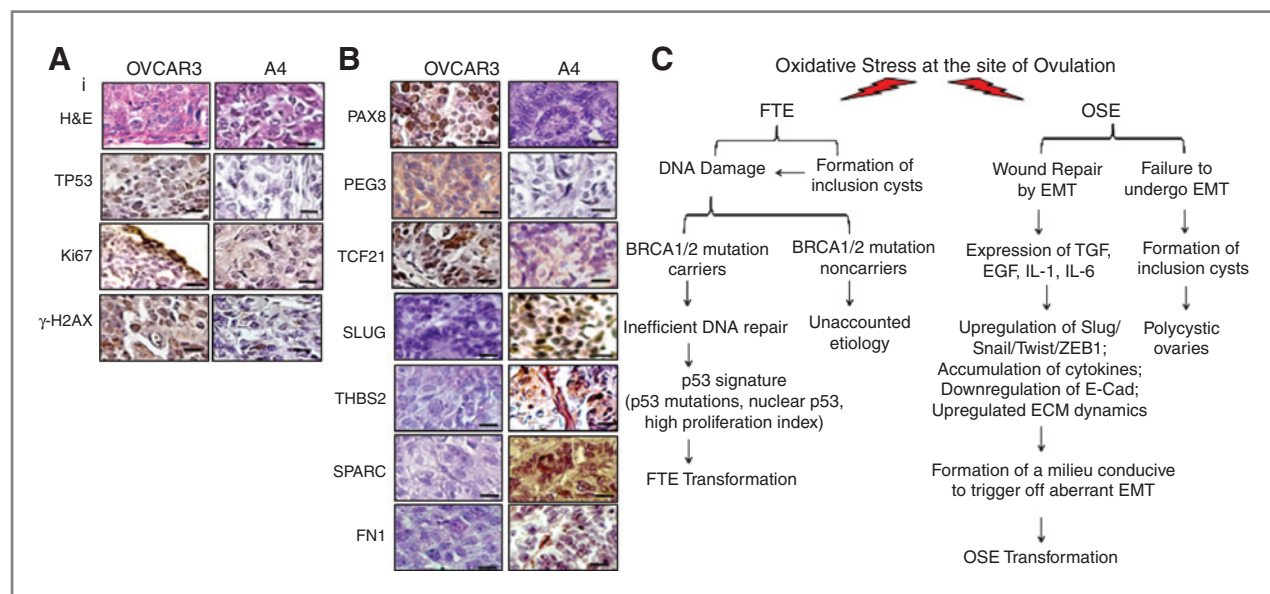
Figure 6. Class-specific features in OVCAR3 and A4 cells. A, p53 signature comprising of TP53, proliferation marker Ki67 and DNA-Damage marker H2AX staining in OVCAR3 (left) and A4 (right) xenografts. H&E (hematoxyline–eosin staining). Scale bar 25 µm; B, representative immunohistochemistry images associated with FTE (Pax8), Stroma (PEG3), MET (TCF21), EMT (Slug), cell migration (THBS2), extracellular matrix proteins (SPARC, FN1); Scale bar-25 µm; C, schematic representation of possible events in transformation of the FTE and OSE triggered by ovulation stress, FTE transformation is brought by activation of a p53 signature, DNA damage, defective DNA repair due to germline BRCA1/2 mutations (in patients) as also modeled in OVCAR3 cells. OSE transformation is a consequence of ECM dynamics and cross-talk initiated by imbalanced release of cytokines and hormones during ovulation that triggers aberrant EMT.

(iv) Cell-specific expression patterns—We further profiled cell-specific expression markers including those of MET - EMT [TCF21 and Slug, respectively; ref. 33), ovarian stroma (PEG3; ref. 34), and secretory FTE (PAX8; ref. 35) in the representative models. A clear association of expression of these markers in OVCAR3 and A4 cells and experimental tumors with the putative etiologies of the two molecular classes was observed (Fig. 6B). We also probed the expression of ECM molecules purported to drive EMT (defined by the Class2-enriched modules M1-M3 association). As expected, Thrombospondin2 (THBS2), Osteonectin (SPARC), and Fibronectin (FN1) were expressed only in Class2 experimental tumors (Fig. 6B). Together, these data provide preliminary support to our hypothesis of differential cell-of-origin between the two classes, with Class1 involving FTE-ovarian stroma cross-talk and Class2 exhibiting features of OSE. However, further validation through lineage tracking and class-affirmation through correlations in patient tumors between all the risk factors from an epidemiologic viewpoint are essential toward a more complete validation of this predicted etiology.

Comparison of the present classification system with other classifiers

Molecular classification of HGSC has been reported earlier; our findings are comparable with and in fact complemented by two recent studies.

Comparing actual tumor samples stratified in our classifier and those in the four HGSC TCGA subtypes (24) revealed Class1 tumors as being either proliferative or differentiated (76.62% and 12.99% respectively), Class2 tumors as mesenchymal or immunoreactive (53.53% & 31.31%, respectively), and Class3 tumors as differentiated or immunoreactive subtypes (54.9% and 25.49% respectively; Supplementary Table S7).

While our manuscript was under compilation, two HGSC classes were reported (36) based on their phenotype as iE and iM classes (epithelial and mesenchymal respectively) resolved through miRNA regulatory network analysis of the TCGA data. Some extent of phenotypic and sample correlation of this classifier with our classes was revealed (Supplementary Table S8). However, although Class1 exhibits epithelial features, our identification of an association of cancer testes antigens, stem cells-, differentiation-, development-, cell cycle-, chromatin modulation- and ovarian function-associated genes suggest unique complementation of cellular programs in this group of tumors that, in the context of metastases, are incapable of undergoing EMT-mediated invasion. Similarly, although our Class2 tumors in direct contrast are EMT-driven, they cannot be assigned a simple "mesenchymal" phenotype since our study also predicts significant cross-talk of the Class2-specific EMT program with extracellular matrix components and other gene networks associated with inflammation, innate/adap-

tive immune mechanisms, escape of tumor cells from immunosurveillance, antigen processing, and IFN responses. Together, all these features contribute to and are crucial determinants of their identity.

Discussion

The relevance of EMT-based signatures as functional classifiers in identification of aggressive disease, and that of genetic instability and CTA expression in the choice of therapy are already established (37, 38). HGSC classification is currently being investigated intensely in view of developing personalized approaches (39). Our approach in the field led to the resolution of three molecular classes, two of which exhibit characteristics that could be important considerations in clinical management. Similarities exist between our classes with earlier relevant classifiers. Comparison with the TCGA subtypes suggests that our classification defines tumors in which the TCGA defined phenotypes may coexist in the same sample, yet assigning such tumors to a single phenotype may be an incomplete assessment of its biological functions. The iE-iM classification on the other hand is a limited description of the biological functions resolved in our stratification as indicated above. Since EMT is a tightly regulated program that is reversed during disease progression in the development of micrometastases (and involves re-establishment of an epithelial phenotype), Class2 tumors can never entirely be considered as being mesenchymal. Furthermore, the fact that a large majority of HGSC tumors present with mixed epithelial–mesenchymal features is overlooked in the iE-iM stratification but are likely to belong to our Class3 and "non-core" samples. Further resolution of such heterogeneity in unclassified samples may be achieved through integration with other functional signatures or profiling differential mechanisms of gene regulation (mutational profiles, methylation, and proteomics) that are increasingly applied in addressing tumor heterogeneity.

On another front, a commonality between some class-specific features and predisposing events of FTE or OSE transformation in HGSC etiology was realized. FTE transformation involves—(i) post-ovulatory oxidative stress, (ii) DNA damage followed by defective repair due to BRCA1/2 mutations in patients that lead to neoplastic changes, genetic instability, and malignant transformation, (iii) precursor lesions characterized by a p53 signature (p53 mutations, high nuclear p53 protein expression and proliferative index), and (iv) expression of the differentiated Müllerian epithelial marker (PAX8) in inclusion cysts within the ovarian stroma. In exploring such features in our experimental models, we did identify high oxidative stress, DNA damage, BRCA2 mutations in its RAD51 binding domain, p53 signature and genetic instability along with PAX8 expression in OVCAR3 cells (Class1). Further association of TCF21 and PEG3 and ovarian functions (steroid hormone biosynthesis—FOXL2, STAR, AMRH2) and germ cell differentiation (CTA) suggests cross-talk between FTE and ovarian stroma, which is supported by earlier reports of

both fallopian tube or ovarian stroma-derived mesenchymal stem cells being capable of MET (40, 41) and niche interactions between preneoplastic lesion–derived FTE and the ovarian cortex being crucial in HGSC (42). Collectively considered, these suggest that Class1 tumors may originate from the FTE (Fig. 6C).

Events associated with OSE transformation include (i) OSE rupture during ovulation accompanied by EGF and TGFβ production triggers a signaling cascade activating Slug/Snail/ZEB1 to initiate EMT-mediated wound healing (42). Incessant ovulation leading to aberrant EMT is thus implicated in OSE transformation (7), (ii) OSE secretes several ECM components, including collagens, integrins, laminins, fibronectin, and vitronectin (43); some of which are implicated in epithelial cell transformation, development of a tumor niche and EMT. These include SPARC (enhanced Slug expression; 44); Decorin (downregulates E-cadherin; 45), Fibronectin (enhanced Slug expression; 46), Periostin (activates Snail *via* β-catenin; 47), and activation of TGF-β (48). The altered ECM milieu thereby triggers an EMT program that generates mesenchymal cells with a capacity of invasion and metastases; such tumor-derived mesenchymal cells contribute to a "mesenchymal" signature. Module M3 enriched in Class2 tumors of our study reflects on such ECM-EMT cross-talk and represents a different modality of metastases from that in the Class1 tumors that are EMT-deficient. (iii) OSE also triggers cytokine production (IL-1, IL-6, G-CSF, M-CSF, GM-CSF) toward follicular growth, differentiation, and ovulation; altered cytokine profiles are associated with transformation (49, 50). Effectively, aberrant derivations of OSE-functions appear to be recapitulated in Class2 tumors as a Slug-ECM-stromal signature, inflammation, IFN signaling and altered host immune responses (Modules M1b, M3, M9; Supplementary Table S5). While their stringent regulation maintain normal organ functioning and homeostasis, these network perturbations in Class2 tumors reflect on intrinsic OSE properties gone awry culminating in transformation (Fig. 6C).

In conclusion, our resolution of HGSC tumor classes generates a much wider and in depth class-specific understanding of the transformation-progression process than that achieved earlier, while their associated networks reveal a novel possibility regarding cell of origin for each class. Further affirmation of the latter through lineage-tracking approaches in elegant disease models are now necessitated to provide affirmation and final validation. Irrespective of this finding, our HGSC stratification has important ramifications toward improving HGSC outcomes through achieving a long-term goal of patient stratification for targeted therapy.

Disclosure of Potential Conflicts of Interest
No potential conflicts of interest were disclosed.

Disclaimer
Publicly available TCGA and GEO datasets were used in this study and are referenced.

Authors' Contributions
Development of methodology: N.L. Gardi, T.U. Deshpande, S.A. Bapat
Acquisition of data (provided animals, acquired and managed patients, provided facilities, etc.): S.C. Kamble, S.R. Budhe
Analysis and interpretation of data (e.g., statistical analysis, biostatistics, computational analysis): N.L. Gardi, T.U. Deshpande, S.C. Kamble, S.R. Budhe, S.A. Bapat
Writing, review, and/or revision of the manuscript: N.L. Gardi, T.U. Deshpande, S.C. Kamble, S.A. Bapat

Acknowledgments

Grant Support

References

1. Kurrey NK, K Amit, Bapat SA. Snail and Slug are major determinants of ovarian cancer invasiveness at the transcription level. Gynecol Oncol 2005;97:155–65.
2. Huber MA, Kraut N, Beug H. Molecular requirements for epithelial-mesenchymal transition during tumor progression. Curr Opin Cell Biol 2005;17:548–58.
3. Moreno-Bueno G, Portillo F, Cano A. Transcriptional regulation of cell polarity in EMT and cancer. Oncogene 2008;27:6958–69.
4. Ahmed N, Thompson EW, Quinn MA. Epithelial-mesenchymal inter-conversions in normal ovarian surface epithelium and ovarian carcinomas: an exception to the norm. J Cell Physiol 2007; 213:581–8.
5. Dorsam RT, Gutkind JS. G-protein-coupled receptors and cancer. Nat Rev Cancer 2007;7:79–94.
6. Samadi N, Bekele R, Capatos D, Venkatraman G, Sariahmetoglu M, Brindley DN. Regulation of lysophosphatidate signaling by autotaxin and lipid phosphate phosphatases with respect to tumor progression, angiogenesis, metastasis and chemo-resistance. Biochimie 2011; 93:61–70.
7. Fathalla MF. Incessant ovulation-a factor in ovarian neoplasia? Lancet 1971;2:163.
8. Auersperg N, Wong AS, Choi KC, Kang SK, Leung PC. Ovarian surface epithelium: biology, endocrinology, and pathology. Endocr Rev 2001; 22:255–88.
9. Lee Y, Miron A, Drapkin R, Nucci MR, Medeiros F, Saleemuddin A, et al. A candidate precursor to serous carcinoma that originates in the distal fallopian tube. J Pathol 2007;211:26–35.
10. Dubeau L. The cell of origin of ovarian epithelial tumours. Lancet Oncol 2008;9:1191–7.
11. Hunn J, Rodriguez GC. Ovarian cancer: etiology, risk factors, and epidemiology. Clin Obstet Gynecol 2012;55:3–23.
12. Folkins AK, Jarboe EA, Saleemuddin A, Lee Y, Callahan MJ, Drapkin R, et al. A candidate precursor to pelvic serous cancer (p53 signature) and its prevalence in ovaries and fallopian tubes from women with BRCA mutations. Gynecol Oncol 2008;109:68–173.
13. Shaw PA, Rouzbahman M, Pizer ES, Pintilie M, Begley H. Candidate serous cancer precursors in fallopian tube epithelium of BRCA1/2 mutation carriers. Mod Pathol 2009;22:1133–8.

14. TCGA. Integrated genomic analyses of ovarian carcinoma. Nature 2011;474:609–15.
15. Bapat SA, Mali AM, Koppikar CB, Kurrey NK. Stem and progenitor-like cells contribute to the aggressive behavior of human epithelial ovarian cancer. Cancer Res 2005;65:3025–9.
16. Kurrey NK, Jalgaonkar SP, Joglekar AV, Ghanate AD, Chaskar PD, Doiphode RY, et al. Snail and Slug mediate radio- and chemo-resistance by antagonizing p53-mediated apoptosis and acquiring a stem-like phenotype in ovarian cancer cells. Stem Cells 2009;27:2059–68.
17. Rousseeuw PJ. Silhouettes: a graphical aid to the interpretation and validation of cluster analysis. J Comput Appl Math 1987;20:53–65.
18. Monti S, Tamayo P, Mesirov J, Golub T. Consensus clustering: a resampling-based method for class discovery and visualization of gene expression microarray data. Mach Learn 2003;52:91–118.
19. Ghazalpour A, Doss S, Zhang B, Wang S, Plaisier C, Castellanos R, et al. Integrating genetic and network analysis to characterize genes related to mouse weight. PLoS Genet 2006;2:e130.
20. Langfelder P, Luo R, Oldham MC, Horvath S. Is my network module preserved and reproducible? PloS Comp Biol 2011;7:e1001057.
21. Subramanian A, Tamayo P, Mootha VK, Mukherjee S, Ebert BL, Gillette MA, et al. Gene set enrichment analysis: a knowledge-based approach for interpreting genome-wide expression profiles. Proc Natl Acad Sci U S A 2005;102:15545–50.
22. Geback T, Schulz MM, Koumoutsakos P, Detmar M. TScratch: a novel and simple software tool for automated analysis of monolayer wound healing assays. Biotechniques 2009;46:265–74.
23. Härmä V, Virtanen J, Mäkelä R, Happonen A, Mpindi JP, Knuuttila M, et al. A comprehensive panel of three-dimensional models for studies of prostate cancer growth, invasion and drug responses. PLoS One 2010;5:e10431.
24. Lizard G, Gueldry S, Sordet O, Monier S, Athias A, Miquet C, et al. Glutathione is implied in the control of 7-ketocholesterol-induced apoptosis, which is associated with radical oxygen species production. FASEB J 1998;12:1651–63.
25. Wani AA, Sharma N, Shouche YS, Bapat SA. Nuclear–mitochondrial genomic profiling reveals a pattern of evolution in epithelial ovarian tumor stem cells. Oncogene 2006;25:6336–44.
26. Bapat SA, Krishnan A, Ghanate AD, Kusumbe AP, Kalra RS. Gene expression: protein interaction systems network modeling identifies transformation-associated molecules and pathways in ovarian cancer. Cancer Res 2010;70:4809–19.
27. Gene omnibus database http://www.ncbi.nlm.nih.gov/geo; 2012.
28. Langfelder P, Horvath S. WGCNA: an R package for weighted correlation network analysis. BMC Bioinformatics 2008;9:559.
29. Margolin AA, Nemenman I, Basso K, Wiggins C, Stolovitzky G, Dalla Favera R, et al. ARACNE: an algorithm for the reconstruction of gene regulatory networks in a mammalian cellular context. BMC Bioinformatics 2006;7 Suppl 1:S7.
30. Rodriguez FJ, Lewis-Tuffin LJ, Anastasiadis PZ. E-cadherin's dark side: possible role in tumor progression. Biochim Biophys Acta 2012;1826:23–31.
31. Yaginuma Y, Westphal H. Abnormal structure and expression of the p53 gene in human ovarian carcinoma cell lines. Cancer Res 1992; 52:4196–9.
32. Donoho G, Brenneman MA, Cui TX, Donoviel D, Vogel H, Goodwin EH, et al. Deletion of Brca2 exon 27 causes hypersensitivity to DNA crosslinks, chromosomal instability, and reduced life span in mice. Genes Chromosomes Cancer 2003;36:317–31.
33. Richards KL, Zhang B, Sun M, Dong W, Churchill J, Bachinski LL, et al. Methylation of the candidate biomarker TCF21 is very frequent across a spectrum of early-stage non-small cell lung cancers. Cancer 2011;117:606–17.
34. Hiby SE, Lough M, Keverne EB, Surani MA, Loke YW, King A. Paternal monoallelic expression of PEG3 in the human placenta. Hum Mol Genet 2001;10:1093–100.
35. Kurman RJ, Shih I. The origin and pathogenesis of epithelial ovarian cancer: a proposed unifying theory. Am J Surg Pathol 2010;34: 433–43.
36. Yang D, Sun Y, Hu L, Zheng H, Ji P, Pecot CV, et al. Integrated analyses identify a master MicroRNA regulatory network for the mesenchymal subtype in serous ovarian cancer. Cell 2013;23:186–99.
37. Taube JH, Herschkowitz JI, Komurov K, Zhou AY, Gupta S, Yang J, et al. Core epithelial-to-mesenchymal transition interactome gene expression signature is associated with claudin-low and metaplastic breast cancer subtypes. Proc Natl Acad Sci U S A 2010; 107:15449–54.
38. Creighton CJ, Li X, Landis M, Dixon JM, Neumeister VM, Sjolund A, et al. Residual breast cancers after conventional therapy display mesenchymal as well as tumor-initiating features. Proc Natl Acad Sci U S A 2009;106:13820–5.
39. Berns EM, Bowtel DD. The changing view of high–grade serous ovarian cancer. Cancer Res 2012;72:2701–4.
40. Kim J, Coffey DM, Creighton CJ, Yu Z, Hawkins SM, Matzuk MM. High-grade serous ovarian cancer arises from fallopian tube in a mouse model. Proc Natl Acad Sci U S A 2012;109:3921–6.
41. Crum CP. Intercepting pelvic cancer in the distal fallopian tube: theories and realities. Mol Oncol 2009;3:165–70.
42. Auersperg N, Maines-Bandiera SL, Dyck HG, Kruk PA. Characterization of cultured human ovarian surface epithelial cells: phenotypic plasticity and premalignant changes. Lab Invest 1994;71:510–8.
43. Kruk PA, Uitto VJ, Firth JD, Dedhar S, Auersperg N. Reciprocal interactions between human ovarian surface epithelial cells and adjacent extracellular matrix. Exp Cell Res 1994;215:97–108.
44. Fenouille N, Tichet M, Dufies M, Pottier A, Mogha A, Soo JK, et al. The Epithelial-Mesenchymal Transition (EMT) regulatory factor SLUG (SNAI2) is a downstream target of SPARC and AKT in promoting melanoma cell invasion. PloS One 2012;7:e40378.
45. Bi XL, Yang W. Biological functions of decorin in cancer. Chin J Cancer 2013;32:266–9.
46. Peng J, Zhang G, Wang Q, Huang J, Ma H, Zhong Y, et al. ROCK cooperated with ET-1 to induce epithelial to mesenchymal transition through SLUG in human ovarian cancer cells. Biosci Biotechnol Biochem 2012;76:42–7.
47. Zhou B, von Gise A, Ma Q, Hu YW, Pu WT. Genetic fate mapping demonstrates contribution of epicardium-derived cells to the annulus fibrosis of the mammalian heart. Dev Biol 2010;338:251–61.
48. Wang H, Zhang H, Tang L, Chen H, Wu C, Zhao M, et al. Resveratrol inhibits TGF-β1-induced epithelial-to-mesenchymal transition and suppresses lung cancer invasion and metastasis. Toxicology 2013;303:139–46.
49. Nash MA, Ferrandina G, Gordinier M, Loercher A, Freedman RS. The role of cytokines in both the normal and malignant ovary. Endocr Relat Cancer 1999;6:93–107.
50. Ziltener HJ, Maines-Bandiera S, Schrader JW, Auersperg N. Secretion of bioactive interleukin-1, interleukin-6, and colony-stimulating factors by human ovarian surface epithelium. Biol Reprod 1993;49:635–41.